

Correcting on-chip distortion of control pulses with silicon spin qubits

Ming Ni(倪铭), Rong-Long Ma(马荣龙), Zhen-Zhen Kong(孔真真), Ning Chu(楚凝), Wei-Zhu Liao(廖伟筑), Sheng-Kai Zhu(祝圣凯), Chu Wang(王儲), Gang Luo(罗刚), Di Liu(刘頔), Gang Cao(曹刚), Gui-Lei Wang(王桂磊), Hai-Ou Li(李海欧), and Guo-Ping Guo(郭国平)

Citation: Chin. Phys. B, 2025, 34 (**1**): 010308. DOI: 10.1088/1674-1056/ad8db1
Journal homepage: http://cpb.iphy.ac.cn; http://iopscience.iop.org/cpb

What follows is a list of articles you may be interested in

Established conversions for hybrid entangled states assisted by error-predicted parity-discriminated devices

Fang-Fang Du(杜芳芳), Zhi-Guo Fan(范志国), Xue-Mei Ren(任雪梅), Ming Ma(马明), and Wen-Yao Liu(刘文耀)
Chin. Phys. B, 2025, 34 (**1**): 010303. DOI: 10.1088/1674-1056/ad8fa0

Coupling and characterization of a Si/SiGe triple quantum dot array with a microwave resonator

Shun-Li Jiang(江顺利), Tian-Yi Jiang(蒋天翼), Yong-Qiang Xu(徐永强), Rui Wu(吴睿), Tian-Yue Hao(郝天岳), Shu-Kun Ye(叶澍坤), Ran-Ran Cai(蔡冉冉), Bao-Chuan Wang(王保传), Hai-Ou Li(李海欧), Gang Cao(曹刚), and Guo-Ping Guo(郭国平)
Chin. Phys. B, 2024, 33 (**9**): 090311. DOI: 10.1088/1674-1056/ad711d

Variational data encoding and correlations in quantum-enhanced machine learning

Ming-Hao Wang(王明浩) and Hua Lü(吕桦)
Chin. Phys. B, 2024, 33 (**9**): 090307. DOI: 10.1088/1674-1056/ad5c3b

Delayed-measurement one-way quantum computing on cloud quantum computer

Zhi-Peng Yang(杨智鹏), Yu-Ran Zhang(张煜然), Fu-Li Li(李福利), and Heng Fan(范桁)
Chin. Phys. B, 2024, 33 (**9**): 090304. DOI: 10.1088/1674-1056/ad6253

Simulations of superconducting quantum gates by digital flux tuner for qubits

Xiao Geng(耿霄), Kaiyong He(何楷泳), Jianshe Liu(刘建设), and Wei Chen(陈炜)
Chin. Phys. B, 2024, 33 (**7**): 070305. DOI: 10.1088/1674-1056/ad47ab

---

Correcting on-chip distortion of control pulses with silicon spin qubits

Ming Ni(倪铭)[1,2,†], Rong-Long Ma(马荣龙)[1,2,†], Zhen-Zhen Kong(孔真真)[3], Ning Chu(楚凝)[1,2], Wei-Zhu Liao(廖伟筑)[1,2], Sheng-Kai Zhu(祝圣凯)[1,2], Chu Wang(王儲)[1,2], Gang Luo(罗刚)[1,2], Di Liu(刘頓)[1,2], Gang Cao(曹刚)[1,2,4], Gui-Lei Wang(王桂磊)[4,5], Hai-Ou Li(李海欧)[1,2,4,‡], and Guo-Ping Guo(郭国平)[1,2,4,6]

[1] *CAS Key Laboratory of Quantum Information, University of Science and Technology of China (USTC), Hefei* 230026, *China*
[2] *CAS Center for Excellence in Quantum Information and Quantum Physics, University of Science and Technology of China, Hefei* 230026, *China*
[3] *Integrated Circuit Advanced Process Research and Development Center, Institute of Microelectronics, Chinese Academy of Sciences (CAS), Beijing* 100029, *China*
[4] *Hefei National Laboratory, Hefei* 230088, *China*
[5] *Beijing Superstring Academy of Memory Technology, Beijing* 100176, *China*
[6] *Origin Quantum Computing Company Limited, Hefei* 230026, *China*

(Received 2 September 2024; revised manuscript received 22 October 2024; accepted manuscript online 1 November 2024)

In semiconductor quantum dot systems, pulse distortion is a significant source of coherent errors, which impedes qubit characterization and control. Here, we demonstrate two calibration methods using a two-qubit system as the detector to correct distortion and calibrate the transfer function of the control line. Both methods are straightforward to implement, robust against noise, and applicable to a wide range of qubit types. The two methods differ in correction accuracy and complexity. The first, coarse predistortion (CPD) method, partially mitigates distortion. The second, all predistortion (APD) method, measures the transfer function and significantly enhances exchange oscillation uniformity. Both methods use exchange oscillation homogeneity as the metric and are suitable for any qubit driven by a diabatic pulse. We believe these methods will enhance qubit characterization accuracy and operation quality in future applications.

Keywords: quantum computation, quantum dot, pulse distortion

PACS: 03.67.Lx, 03.67.–a, 68.65.Hb

DOI: 10.1088/1674-1056/ad8db1 **CSTR:** 32038.14.CPB.ad8db1

1. Introduction

Universal quantum computation requires both single-qubit and two-qubit gates with long coherence times and high gate fidelities.[1–4] For qubits defined in semiconductor quantum dots, accurately delivering the control waveform to the device is essential for successful gate operations.[5–7] Optimizing the control waveform is a widely used method to enhance gate fidelity during qubit gate implementations.[8–12] However, waveform distortion is inevitable in the measurement system, which hinders the achievement of high-fidelity qubit gates and sequences.[8,13–15] Additionally, an accurate measurement pulse is crucial for system characterization, such as noise measurements[16,17] and energy-level structure analysis.[18,19]

Pulse distortion in the measurement system can arise from factors like limited arbitrary waveform generator (AWG) bandwidth, filtering effects, skin effect, and impedance mismatch. In general, pulse distortion can be described by a transfer function $h(t)$, which captures the influence of all distortion sources along the control line, from room temperature electronics to the qubit on the chip. Once the transfer function is calibrated, predistortion corrections can be applied to the control pulse to compensate for the distortion. While pulse distortion can be easily measured at room temperature using a vector network analyzer or oscilloscope, at cryogenic temperatures, qubits are often used as sensors to detect the response of control pulses.

For superconducting qubits, various techniques have been developed to calibrate waveform distortion.[20–26] Similarly, for spin qubits in semiconductor quantum dots, previous efforts have aimed to eliminate pulse distortion in the control line. In singlet-triplet (ST) qubits, used as detectors, gate fidelities are optimized using the Levenberg–Marquardt algorithm (LMA) to mitigate both decoherent noise and pulse distortion.[27–29] However, in these works, distortion is calibrated alongside noise, making it difficult to separately address pulse distortion. Another approach uses phase accumulation during exchange oscillation as an indicator to estimate the system transfer function, but this method is sensitive to noise and effective only over short time intervals.[30]

In this article, we propose two methods to calibrate pulse distortion in a two-qubit system using exchange oscillation as the detector. These methods provide the system's transfer function and calibrate distortion over both short (∼ns) and long (∼ μs) time intervals, making them applicable in a range

†These authors contributed equally to this work.
‡Corresponding author. E-mail: haiouli@ustc.edu.cn

© 2025 Chinese Physical Society and IOP Publishing Ltd. All rights, including for text and data mining, AI training, and similar technologies, are reserved.

of scenarios.[8,13–19] The first method, coarse predistortion (CPD), primarily corrects distortion caused by the bias-tee by using the frequency spectrum width of the oscillation as a calibration standard. The second method, all predistortion (APD), offers higher correction accuracy and but more complexity by using oscillation pole positions as the standards to calibrate the system's transfer function. With the corrected waveform, we observed a significant improvement in exchange oscillation uniformity, demonstrating the effectiveness of these calibration procedures.

2. Results

2.1. Experimental setup

We conduct our experiment on a gate-defined two-qubit device fabricated on a 70-nm isotopically purified ^{28}Si epilayer.[31–33] As depicted in Fig. 1(a), the left qubit $Q_{\rm L}$ and right qubit $Q_{\rm R}$ are positioned beneath the plunger gates PL and PR, respectively. Electrons tunnel between the quantum dots and the electron reservoir beneath gate RG, with the tunneling rate controlled by the voltage on gate BL. DC voltages applied to the plunger gates create potential wells that confine the electrons. Our experiments are performed in the (3,1) charge configuration under an external magnetic field $B_0 = 605$ mT. Both qubits are read out and initialized as described in Ref. [34]. Qubit $Q_{\rm L}$ is directly read out and initialized via spin-selective tunneling with the left reservoir. However, $Q_{\rm R}$ has a slower tunneling rate and requires spin shuttling to the left quantum dot for readout and initialization. The detuning ε between the two qubits is controlled by adjusting the relative voltages on PL and PR, and the tunnel coupling $t_{\rm c}$ is tuned by the gate voltage on BR.

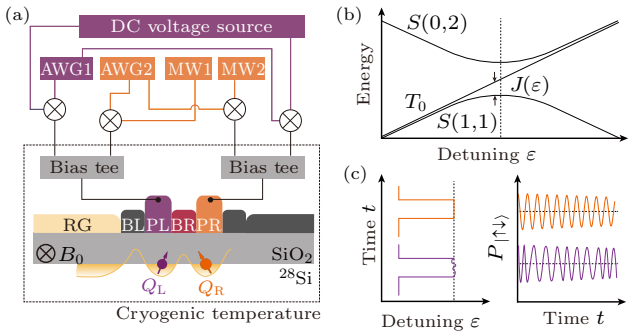


Fig. 1. (a) Schematic diagram of the measurement system and device. The pulse on the order of kHz is generated by AWG1 overlaps with the DC voltage. And the pulse on the order of GHz is generated by AWG2 and overlaps with the microwave. At cryogenic temperature, two bias tees combine all control signals and deliver them to the plunger gates PL and PR, respectively. The two qubits $Q_{\rm L}$ and $Q_{\rm L}$ are located underneath the two plunger gates and are directly controlled by the signal output from the bias tees. (b) Energy-level diagram of the two-qubit system as a function of the detuning ε. ε is controlled by the relative voltage between PL and PR. The exchange coupling $J(\varepsilon)$ is the energy splitting between the singlet and triplet states. (c) Illustration of the exchange oscillation corresponding to the undistorted (orange) and distorted (purple) pulses. The exchange oscillation frequency $f_{\rm ex}$ is proportional to the pulse amplitude at time t.

Figure 1(a) also illustrates the measurement setup. Our system requires control signals ranging from kHz for single-shot readout and initialization to GHz for single-qubit and two-qubit gate operations. Two arbitrary waveform generators (AWGs) are used: AWG1 generates kHz pulses, while AWG2 generates GHz pulses. Additionally, two vector microwave sources (MW1 and MW2) drive qubits $Q_{\rm L}$ and $Q_{\rm R}$, respectively. To simultaneously deliver both pulses and microwaves to the device, two bias tees are connected to the plunger gates at cryogenic temperatures. The kHz pulse is combined with the DC voltage at room temperature and delivered via the DC port of the bias tee, while the GHz pulse is combined with the microwaves and delivered via the RF port. Among the input signals, distortion in the GHz pulses, introduced through the RF port, impacts the qubit control. In this work, we focus on correcting GHz pulse distortions to improve the performance of two-qubit gate operations.

2.2. Exchange oscillation

For the two qubits $Q_{\rm L}$ and $Q_{\rm R}$ formed in two adjacent quantum dots, their Zeeman splitting energies $E_{\rm z}$ differ due to the Stark shift.[5–7,35] Meanwhile, the exchange coupling J is always present and can be tuned by the detuning ε. Here, we focus on the basis of antiparallel states $|\uparrow\downarrow\rangle$ and $|\downarrow\uparrow\rangle$, with the Hamiltonian given by

$$H = \Delta E_{\rm z}\sigma_z + J\sigma_x, \tag{1}$$

where $\Delta E_{\rm z}$ is the Zeeman splitting energy difference for the two qubits. As mentioned earlier, the detuning ε between the two qubits can be adjusted by the relative gate voltages $V_{\rm PL}$ and $V_{\rm PR}$. When diabatic pulses are applied to the plunger gates, the two-qubit state remains static while the eigenstates evolve due to the modified ε, as illustrated in Fig. 1(b).[37] The exchange coupling oscillation will occur between the two qubits, with a frequency equal to the energy difference between the two antiparallel eigenstates, given by $f_{\rm ex} = \sqrt{\Delta E_{\rm z}^2 + J^2}$.[34] In our device, since $J \propto \exp(\varepsilon)$[6] and $\Delta E_{\rm z} \propto \varepsilon$ we should observe a homogeneous exchange oscillation with frequency $f_{\rm ex}$ as long as the top edge of the diabatic pulse is flat. If the two qubits are initialized to the state $|\uparrow\downarrow\rangle$, figure 1(c) illustrates the oscillation of the probability of the state $|\uparrow\downarrow\rangle$ driven by both undistorted and distorted pulses. A slight distortion at the top edge will alter the pulse amplitude as well as ε at the operational point, leading to a change in $f_{\rm ex}$ and resulting in apparent inhomogeneous oscillation. In our experiment, when the top edge of the fast pulse is flat, we observe a gradual slowdown in the exchange oscillation frequency, as shown in the un-predistorted (UPD) situation in Fig. 4(a). This indicates that the control pulse is distorted and that the top edge decays over time. We attribute this distortion to the RC filter circuit within the bias tee, which causes the top edge of the square pulse to decay.

2.3. CPD method

The pulse affected by the RC filter circuit is illustrated in Fig. 2(a). For a diabatic square input pulse $U_{\rm in}(t)$, the output pulse after passing through the circuit is denoted as $U_{\rm out}(t)$), which serves as the control signal for the two qubits. In the absence of distortion from the circuit, $U_{\rm out}(t)$ would initially rise and then maintain a stable amplitude $A_{\rm in}$, matching the amplitude of $U_{\rm in}(t)$. However, when distorted by the RC filter circuit, $U_{\rm out}(t)$ will behave differently. After the rising edge, the output pulse $U_{\rm out}(t)$ will experience exponential decay at the top edge due to the circuit distortion, following the form $U_{\rm out}(t) = A_{\rm in}\,{\rm e}^{-t/\tau}$, where t is the duration time of the top edge and τ is the time constant of the RC filter circuit, which depends on the values of the capacitor and resistor in the RC circuit. Subsequently, after the falling edge, $U_{\rm out}(t)$ will drop sharply and then rise exponentially to zero. To fully compensate the $U_{\rm out}(t)$ into a diabatic square pulse, the input pulse should has the form $U_{\rm in}(t) = A_{\rm in}(1+kt)$. In our experiment, to predistort $U_{\rm in}(t)$, we employ a pulse with a linearly ramped top edge given by $U_{\rm PD,in}(t) = A_{\rm in}(1+kt)$ where k is a constant that determines the slope of the ramp. As illustrated in Fig. 2(a), this linearly ramped top edge can effectively compensate for the decay induced by the RC filter circuit. To achieve complete correction of the bottom edge, the predistorted pulse must maintain a nonzero voltage level of $A_{\rm in}kt$ after the falling edge. Considering the inevitable return to a zero voltage level following the falling edge, we linearly decrease the voltage to this zero-voltage level and neglect the effect of any remaining distortion.

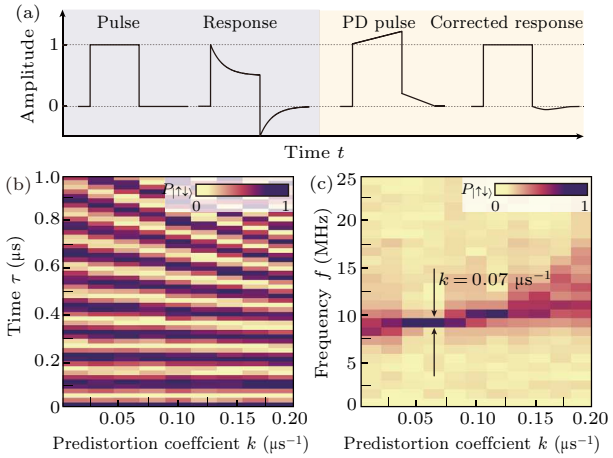


Fig. 2. (a) Schematic diagram of the square pulse response after the RC filter circuit inside the bias tee. The predistorted (PD) pulse with a linearly ramped top edge can correct the distortion. A linear ramped down pulse after the falling edge is utilized to gradually decrease the pulse amplitude to zero and lower the influence of the remaining distortion as much as possible. (b) Time-dependent responses of the spin-up probability of the $|\uparrow\downarrow\rangle$ state with the predistorted pulse. The oscillation frequency significantly increases as the predistortion coefficient k increases. The frequency spectroscopy in panel (c) gives the Fourier transformation of panel (b). The narrow FHWM around $k = 0.07$ μs^{-1} indicates improved oscillation homogeneity.

To detect the ramp rate k, we measure the exchange oscillation as k increases. The time domain behavior of the oscillation with increasing k is shown in Fig. 2(b). The spin-up probability $P_{|\uparrow\downarrow\rangle}$ exhibits inhomogeneous oscillations over time. To characterize this inhomogeneity, we transform the data from Fig. 2(b) into the frequency domain, allowing us to assess the homogeneity of the exchange oscillation. The frequency spectroscopy is presented in Fig. 2(c). When k is approximately 0.06 μs^{-1} to 0.08 μs^{-1}, the spread of the frequency peak is at its narrowest, indicating that the oscillation homogeneity is optimized. Consequently, we select $k = 0.07$ μs^{-1} for subsequent experiments, which corresponds to a time constant of $\tau \approx 1/k \approx 14$ μs for the RC circuit. Although the linearly ramped top edge mitigates some distortion, the exchange oscillation remains disturbed when the oscillation frequency exceeds 20 MHz, as demonstrated in the CPD situation shown in Figs. 4(a) and 4(b). This observation suggests that residual distortion still impacts the oscillation, indicating the necessity for a more precise calibration method.

2.4. APD method

In the regime of $J \gg \Delta E_z$, the exchange oscillation frequency $f_{\rm ex} \approx J(\varepsilon)$ due to the exponential dependence between J and ε. As $A_{\rm in}$ increases, ε at the operation point increases as well, and the exchange oscillation frequency increases exponentially.[6] Therefore, the higher the $A_{\rm in}$ is, the more sensitive the $f_{\rm ex}$ is to pulse distortion. A natural thought is calibrating the control pulse according to the accumulated exchange oscillation phase. However, the phase is susceptible to decoherence and the spin preparation and measurement (SPAM) error. In contrast, the extremum points where the phases are equal to $n\cdot\pi$ ($n = 1, 2, 3, \ldots$) have decoherence and SPAM error insensitive performance and are suitable as the distortion metric. In our experiment, we adjust $A_{\rm in}$ and choose a fixed pulse duration λ to obtain the predistorted pulse. When $U_{\rm in}(t)$ is not disturbed, $2\pi f_{\rm ex}(A_{\rm in})\,\lambda = \pi$ (or 2π), and the spin-up probability $P_{|\uparrow\downarrow\rangle}$ will reach extremum points at time $t = n\cdot\lambda$ ($n = 1, 2, 3, \ldots$). With the distortion, while making $P_{|\uparrow\downarrow\rangle}$ still reach extremum points at the moment t, we need to adjust $A_{\rm in}$ of $U_{\rm in}(t)$ during each time segment λ. After modifying the $A_{\rm in}$ of $U_{\rm in}(t)$, we can obtain the $U_{\rm in}(t)$, which corresponds to a square wave output pulse $U_{\rm out}(t)$. Although the pulse distortion will also influence the falling edge, due to the nonlinear dependence between the pulse amplitude and the exchange oscillation frequency/axis angle and the compensated pulse in Fig. 2(b), the influence of the pulse distortion during the falling edge can be neglected, we can only focus on calibrating the distortion in the rising edge (see supplementary material 4 for more detail).

Before correcting the control pulse, we calibrate the relationship between $f_{\rm ex}$ and $A_{\rm in}$ (see supplementary material 1 for more detail), with which we can determine the un-distorted $A_{\rm in}$ corresponding to $f_{\rm ex}(A_{\rm in}) = \pi/\lambda$ (or $f_{\rm ex}(A_{\rm in}) = 2\pi/\lambda$). The

following steps summarize the experimental procedures.

(i) According to the dependence between $f_{\rm ex}$ and $A_{\rm in}$, we calculate the $A_{\rm in,1}$ that makes the accumulated phase ϕ_{λ_1} equal to π (2π) at time λ_1. Here, λ_1 is the fixed temporal resolution of the calibration procedure, and we assume that the output voltage level during λ_1 is constant. For example, in Figs. 3(a) and 3(b), we chose the $A_{\rm in,1}$ corresponding to $f_{\rm ex} = 10$ MHz when ensuring $\lambda_1 = 0.1$ μs to guarantee $\phi_{\lambda_1} = 2\pi$.

(ii) Keep the input square pulse duration as λ_1 and set the pulse amplitude as $c_{11}A_{\rm in,1}$, where c_{11} is the predistortion coefficient. Sweep c_{11} around 1 and find the predistortion coefficient c_{11}, which corresponds to the extremum value of $P_{|\uparrow\downarrow\rangle}$. As illustrated in Figs. 3(a) and 3(b), c_{11} is swept in the interval [0.95, 1.05] and chosen as the value corresponding to the maximum $P_{|\uparrow\downarrow\rangle}$.

(iii) Keep the input square pulse $U_{\rm in}(t)$ duration as $2\lambda_1$ and set the pulse amplitude in the time interval $[0,\lambda_1]$ as $c_{11}A_{\rm in,1}$. In the time interval $[\lambda_1, 2\lambda_1]$, we set the pulse amplitude as $c_{12}A_{\rm in,1}$ and sweep c_{12} around 1 to find c_{12} that corresponds to the extremum value of $P_{|\uparrow\downarrow\rangle}$.

(iv) Repeat Step (iii) and determine $c_1 = [c_{11}, c_{12}, c_{13}, \ldots, c_{1n}]$. The orange pulse segments in Figs. 3(a) and 3(b) correspond to the calibrated $c_1 = [c_{11}, c_{12}, c_{13}, \ldots, c_{110}]$.

(v) To increase the calibration temporal resolution, decrease the calibration duration step λ_2, calculate $A_{\rm in,2}$ and repeat Steps (i)–(iv) to determine the value of c_2. Before this step, set $U_{\rm in}(t)$ as $c_1 u(t)$, and $u(t)$ is the square pulse with amplitude $A_{\rm in,1}$. In Figs. 3(c) and 3(d), we chose $\lambda_2 = 0.05$ μs, $f_{\rm ex} = 20$ MHz, and $\phi_{\lambda_2} = 2\pi$. The calibration of c_2 is based on the calibrated pulse in Fig. 3(b).

(vi) Decrease the calibration duration step λ_m and calibrate $c_m = [c_{m1}, c_{m2}, c_{m3}, \ldots, c_{mn}]$ until the temporal resolution is sufficient.

(vii) Calculate the predistorted input pulse as $U_{\rm in}(t) = c_1\ c_2\ \ldots\ c_m u(t)$. Finally, we obtain $U_{\rm in}(t)$, which ensures that the pulse delivered into device $U_{\rm out}(t)$ is an exact square pulse.

The APD input pulse $U_{\rm in,APD}(t)$ in our experiment is shown in Fig. 3(e). As the contrasts, we also give the CPD pulse $U_{\rm in,CPD}(t)$ with a line ramped top edge and the initial square pulse $U_{\rm in,UPD}(t)$. Two rounds of iterations with $\lambda_1 = 40$ ns and $\lambda_2 = 20$ ns are implemented successively to obtain $U_{\rm in,APD}(t)$. The phase step is π, and the sweeping interval of c is $[0.85, 1.15]$. During the duration [0 ns, 80 ns], the pulse amplitude of $U_{\rm in,APD}(t)$ is lower than that of $U_{\rm in,CPD}(t)$ which should correspond to the lower oscillation frequency. In Fig. 4(a), in comparison to the exchange oscillation driven by $U_{\rm in,CPD}(t)$, we observe that the exchange oscillation driven by $U_{\rm in,APD}(t)$ is indeed slower and more homogeneous. Similarly, the pulse amplitude of $U_{\rm in,APD}(t)$ within time [80 ns, 220 ns] is higher, which also improves the oscillation homogeneity compared to $U_{\rm in,CPD}(t)$. The significant conformity confirms the validity of this procedure. Although the trend is corrected, $U_{\rm in,APD}(t)$ in Fig. 4(c) is still disturbed by some glitches due to the exchange oscillation instability. To smooth these glitches, we fit $U_{\rm in,APD}(t)$ with a polynomial curve. We speculate that the glitch problem can be relieved by averaging more time during the calibration or with a higher quality exchange oscillation.

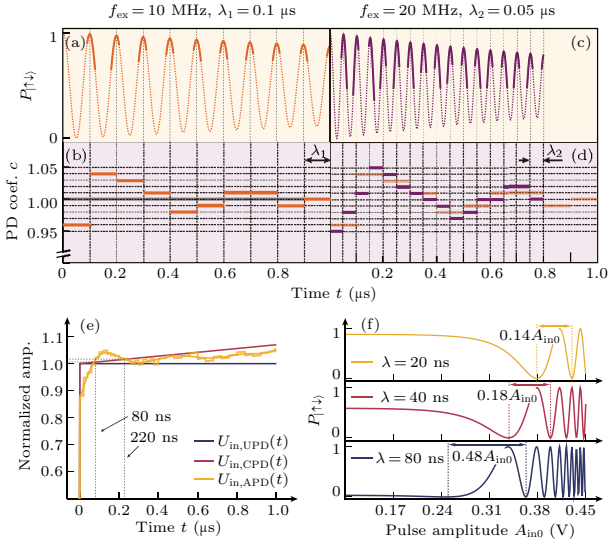


Fig. 3. (a)–(d) Schematic diagram of our calibration procedure. The spin-up probability $P_{|\uparrow\downarrow\rangle}$ is measured as a function of the predistortion coefficient (PD coef.) c. During each time interval λ_n, c_n is chosen to maximize $P_{|\uparrow\downarrow\rangle}$, and the amplitude (amp.) of $U_{\rm in}(t)$ is adjusted to $c_n \cdot A_{\rm in}$. Here are two rounds of calibration that chose the phase step ϕ_λ as 2π and the sweeping interval of the pulse amplitude as ±15%. According to the characteristics of exchange oscillation, we apply $\lambda_1 = 0.1$ μs, $n_1 = 10$, $\lambda_2 = 0.05$ μs and $n_2 = 16$. (e) The initial square pulse $U_{\rm in,UPD}(t)$ (blue), the coarse predistorted pulse (CPD) $U_{\rm in,CPD}(t)$ (red), and the all predistorted input pulse $U_{\rm in,APD}(t)$ (yellow). All of them are experimentally measured. The linearly ramped rate k of $U_{\rm in,CPD}(t)$ is 0.07 μs^{-1}. The rough yellow line represents the directly calibrated $U_{\rm in,APD}(t)$ in our experiment. Two rounds of iterations with $\lambda_1 = 40$ ns and $\lambda_2 = 20$ ns are implemented to calibrate $U_{\rm in,APD}(t)$. The smooth yellow line corresponds to the polynomial curve fitted $U_{\rm in,APD}(t)$, which relieves the glitches of the directly calibrated one. The dashed lines indicate the time at 80 ns and 220 ns, correspond to where $U_{\rm in,CPD}(t) = U_{\rm in,APD}(t)$. All three pulses are normalized. (f) Schematic diagram of the multipeak phenomenon during calibration. As $A_{\rm in}$ is modified, the smaller temporal resolution λ corresponding to a larger $f_{\rm ex}$ is more susceptible to the multipeak phenomenon. The colored dashed lines indicate $A_{\rm in}$, where the accumulated phase equals π and 3π, respectively.

Although the validity is confirmed, this calibration procedure still has some limitations, predominantly in the temporal resolution, longest correction time, and accuracy, and is mainly influenced by the exchange oscillation characteristics. Specifically, the temporal resolution λ_m depends on the fastest exchange oscillation frequency, and the coherence time of the exchange oscillation determines the longest correction time $n \cdot \lambda_m$ our procedure can calibrate. The accuracy of this procedure is dominated by the phase step we choose; in other words, the larger the phase step we choose, the more susceptible the extremum point is. However, for the same λ_m, a larger phase step means that a higher $f_{\rm ex}$ is needed, which is often accompanied by a faster decoherence speed and results in a shorter correction time. Thus, these parameters should be chosen carefully.

Remarkably, two situations could lead to the failure of the APD procedure. The first is the occurrence of multiple peaks within the scanning interval of c. As illustrated in Fig. 3(f), when modifying c_{mn}, we observed a gradual increase in the oscillation frequency. For different pulse durations λ shown in Fig. 3(f), the latest extremum points are detected when $A_{\text{in}0}$ shifts by $0.48A_{\text{in}0}$, $0.18A_{\text{in}0}$, and $0.14A_{\text{in}0}$, respectively. Here, $A_{\text{in}0}$ denotes the ideal pulse amplitude corresponding to the extremum point. A higher temporal resolution, along with a smaller λ, is more likely to lead to multiple peaks. When the sweep interval is excessively large, multiple peaks may emerge, resulting in a misleading determination of c_{mn}. The second situation that can lead to the failure of the APD procedure occurs when the distortion is so severe that we detect the wrong probability peak. Paradoxically, while a narrow sweeping interval for c_{mn} is recommended to avoid the multiple peak phenomenon, it may cause us to miss the extremum point when the distortion is significant. To address this, we propose starting with a longer temporal resolution and a larger λ, which typically corresponds to a smaller average distortion and reduced disturbance from the multiple peak phenomenon. This approach allows us to select a narrower sweeping interval, which we can then refine by increasing the resolution during multiple iterations. Alternatively, employing the CPD procedure before the APD procedure can also be beneficial. In general, careful selection of the temporal resolution, $\lambda_{m,n}$, and c is crucial to ensure the validity of the calibration procedure, based on the characteristics of the exchange oscillation.

With $U_{\text{in,APD}}(t)$, we can easily calculate the transfer function $h(t)$ and the inverse transfer function $h^{-1}(t) = U'_{\text{in,APD}}(t)$, allowing us to obtain the predistorted pulse for any arbitrary output pulse $U_{\text{in,APD}}(t) = h^{-1}(t) \cdot U_{\text{out}}(t)$ (see supplementary material 2 for more details). In Fig. 4(a), we demonstrate the time dependence of the exchange oscillation using $U_{\text{in,UPD}}(t)$, $U_{\text{in,CPD}}(t)$, and $U_{\text{in,APD}}(t)$ as a function of A_{in}. To illustrate the homogeneity of the oscillation, we transform the exchange oscillation from the time domain to the frequency domain, as shown in Fig. 4(b). When the UPD pulse $U_{\text{in,UPD}}(t)$ is applied to the qubits, as A_{in} increases, the frequency spectrum of the exchange oscillation becomes unclear. As previously mentioned, f_{ex} gradually slows down over time, primarily affected by the RC filter circuit. Consequently, we correct the distortion with a linear ramp top edge. In Fig. 4(b), under the CPD situation, the frequency spectroscopy improves when f_{ex} is below 20 MHz, but it remains unclear at higher frequencies. This indicates that while the distortion is partially mitigated, the influence of the residual distortion is still apparent. With the APD procedure, the frequency spectroscopy remains clear even when f_{ex} exceeds 20 MHz, leading to a significant improvement in homogeneity. The residual width of the frequency peak is attributed to oscillation decoherence and low temporal resolution, which is approximately 50 MHz in this case.

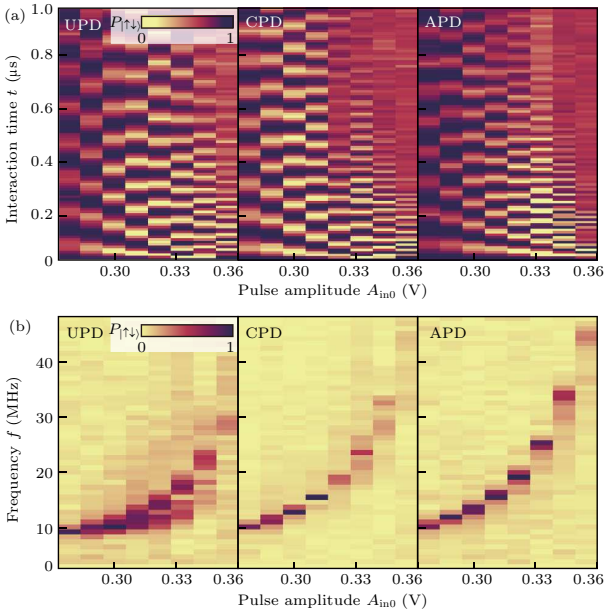


Fig. 4. (a) The time dependence of the exchange oscillation between the $|\uparrow\downarrow\rangle$ and $|\downarrow\uparrow\rangle$ states of two spin qubits driven with the UPD pulse $U_{\text{in,UPD}}(t)$, the CPD pulse $U_{\text{in,CPD}}(t)$, and the APD pulse $U_{\text{in,APD}}(t)$. (b) Frequency spectroscopy is obtained by transferring the exchange oscillation in panel (a) into the frequency domain.

3. Discussion

The calibrated pulse is essential for characterizing coherence time and identifying error sources. Compared to the CPD method, the APD procedure focuses on calibrating distortions in the first few oscillations, which is critical for enhancing gate fidelity. The APD method's temporal resolution is determined by the highest oscillation frequency (in the GHz range), which easily meets the sub-microsecond pulse requirements for gate operations. Although higher oscillation frequencies provide better temporal resolution, optimal gate fidelity is achieved at slower oscillation frequencies. By calibrating distortion during the initial oscillations, gate fidelity can be improved even at intermediate operation points or during $\pi/2$ rotations. When choosing between the CPD and APD methods, experimental requirements play a key role. The CPD method offers faster calibration but at the cost of precision, while the APD method, through iterative processes, delivers higher accuracy. For oscillation frequencies below 20 MHz, the calibration accuracy of both methods is comparable, and deviations in peak frequency width may result from unaveraged disturbances. Therefore, CPD is suitable for experiments prioritizing speed, while APD is better suited for those requiring higher precision.

In our experiment, both predistortion methods exhibit noise immunity and can effectively calibrate over long time intervals. For exchange oscillation, the primary source of error is quasi-static charge noise, which leads to decoherence.

However, decoherence does not compromise the calibration accuracy of either predistortion method, allowing us to calibrate pulse distortion for longer pulses. In the CPD method, while decoherence broadens the frequency spectrum of the oscillation, this band spread does not invalidate the CPD method since the predistortion coefficient k corresponds to the relatively narrowest band. For the APD method, we determine pulse distortion using extremum points; both the pulse amplitude and duration associated with these extremum points exhibit noise immunity and remain unaffected by oscillation decoherence. Benefiting from these factors, we can utilize these methods to enhance control pulses not only for gate operations[8,13–15] but also for system characterization.[16–19]

On a larger scale, both the CPD and APD methods can be applied to calibrate pulse distortion for various types of qubit encodings and substrate materials, with the only requirement being oscillation driven by a diabatic pulse. For instance, leveraging the exchange interaction between qubits, the exchange oscillation observed through Elzerman readout or Pauli spin-blockade (PSB) readout serves as an excellent mechanism for calibrating pulse distortion in single-spin qubits, singlet-triplet (ST) qubits, exchange-only qubits, and donor-based qubits encoding electron spins. The diabatic pulse can be applied to both ε and t_c. Additionally, the oscillation driven by the diabatic pulse on ε can stem from spin–orbit coupling or spin–valley coupling. The calibrated pulse can further enhance the operation of hybrid spin–valley qubits. Beyond qubits based on silicon MOS, these two methods can also be effective for qubit encodings on different substrate materials, such as SiGe/Si, GeSi/Ge, nanowires, and FinFET.

4. Summary

In summary, we demonstrated two distinct methods for calibrating distortion in our system by using the two-qubit exchange oscillation in a silicon metal–oxide–semiconductor (MOS) quantum dot as the detector. The CPD procedure, which features a linear ramp top edge, rapidly calibrates distortion originating from the bias tee. Meanwhile, the APD procedure, which uses the extremum value of $P_{|\uparrow\downarrow\rangle}$ as a metric, characterizes the transfer function of the measurement system. We observed a significant improvement in the homogeneity of exchange oscillation with the transfer function across all frequency ranges. These methods are straightforward and suitable for any qubit system exhibiting oscillation driven by a diabatic square pulse. We believe this correction procedure has the potential to enhance gate fidelity and system characterization in future experiments.

Acknowledgements

Project supported by the National Natural Science Foundation of China (Grant Nos. 12074368, 92165207, 12474490, 12034018, and 92265113), the Innovation Program for Quantum Science and Technology (Grant No. 2021ZD0302300), and the USTC Tang Scholarship. This work was partially carried out at the USTC Center for Micro and Nanoscale Research and Fabrication.

References

[1] DiVincenzo D P 2000 *Fortschritte der Physik* **48** 771
[2] Burkard G, Ladd T D, Pan A, Nichol J M and Petta J R 2023 *Rev. Mod. Phys.* **95** 025003
[3] Zhang X, Li H O, Cao G, Xiao M, Guo G C and Guo G P 2019 *National Science Review* **6** 32
[4] Zwanenburg F A, Dzurak A S, Morello A, Simmons M Y, Hollenberg L C L, Klimeck G, Rogge S, Coppersmith S N and Eriksson M A 2013 *Rev. Mod. Phys.* **85** 961
[5] Veldhorst M, Yang C H, Hwang J C C, Huang W, Dehollain J P, Muhonen J T, Simmons S, Laucht A, Hudson F E, Itoh K M, Morello A and Dzurak A S 2015 *Nature* **526** 410
[6] Watson T F, Philips S G J, Kawakami E, Ward D R, Scarlino P, Veldhorst M, Savage D E, Lagally M G, Friesen M, Coppersmith S N, Eriksson M A and Vandersypen L M K 2018 *Nature* **555** 633
[7] Zajac D M, Sigillito A J, Russ M, Borjans F, Taylor J M, Burkard G and Petta J R 2018 *Science* **359** 439
[8] Xue X, Russ M, Samkharadze N, Undseth B, Sammak A, Scappucci G and Vandersypen L M K 2022 *Nature* **601** 343
[9] Noiri A, Takeda K, Nakajima T, Kobayashi T, Sammak A, Scappucci G and Tarucha S 2022 *Nature* **601** 338
[10] Mills A R, Guinn C R, Gullans M J, Sigillito A J, Feldman M M, Nielsen E and Petta J R 2022 *Sci. Adv.* **8** eabn5130
[11] Yang C H, Chan K W, Harper R, Huang W, Evans T, Hwang J C C, Hensen B, Laucht A, Tanttu T, Hudson F E, Flammia S T, Itoh K M, Morello A, Bartlett S D and Dzurak A S 2019 *Nature Electronics* **2** 151
[12] Takeda K, Yoneda J, Otsuka T, Nakajima T, Delbecq M R, Allison G, Hoshi Y, Usami N, Itoh K M, Oda S, Kodera T and Tarucha S 2018 *Npj Quantum Inform.* **4** 54
[13] Petit L, Russ M, Eenink G H G J, Lawrie W I L, Clarke J S, Vandersypen L M K and Veldhorst M 2022 *Communications Materials* **3** 82
[14] Takeda K, Noiri A, Nakajima T, Kobayashi T and Tarucha S 2022 *Nature* **608** 682
[15] Weinstein A J, Reed M D, Jones A M, Andrews R W, Barnes D, Blumoff J Z, Euliss L E, Eng K, Fong B H, Ha S D, Hulbert D R, Jackson C A C, Jura M, Keating T E, Kerckhoff J, Kiselev A A, Matten J, Sabbir G, Smith A, Wright J, Rakher M T, Ladd T D and Borselli M G 2023 *Nature* **615** 817
[16] Struck T, Hollmann A, Schauer F, Fedorets O, Schmidbauer A, Sawano K, Riemann H, Abrosimov N V, Cywiński Ł, Bougeard D and Schreiber L R 2020 *Npj Quantum Inform.* **6** 40
[17] Kawakami E, Jullien T, Scarlino P, Ward D R, Savage D E, Lagally M G, Dobrovitski V V, Friesen M, Coppersmith S N, Eriksson M A and Vandersypen L M K 2016 *Proc. Natl. Acad. Sci.* **113** 11738
[18] Cai X, Connors E J, Edge L F and Nichol J M 2023 *Nat. Phys.* **19** 386
[19] Gilbert W, Tanttu T, Lim W H, Feng M, Huang J Y, Cifuentes J D, Serrano S, Mai P Y, Leon R C C, Escott C C, Itoh K M, Abrosimov N V, Pohl H J, Thewalt M L W, Hudson F E, Morello A, Laucht A, Yang C H, Saraiva A and Dzurak A S 2023 *Nat. Nanotechnol.* **18** 131
[20] Bylander J, Rudner M S, Shytov A V, Valenzuela S O, Berns D M, Berggren K K, Levitov L S and Oliver W D 2009 *Phys. Rev. B* **80** 220506
[21] Gustavsson S, Zwier O, Bylander J, Yan F, Yoshihara F, Nakamura Y, Orlando T P and Oliver W D 2013 *Phys. Rev. Lett.* **110** 040502
[22] Jerger M, Kulikov A, Vasselin Z and Fedorov A 2019 *Phys. Rev. Lett.* **123** 150501
[23] Rol M A, Ciorciaro L, Malinowski F K, Tarasinski B M, Sagastizabal R E, Bultink C C, Salathe Y, Haandbaek N, Sedivy J and DiCarlo L 2020 *Appl. Phys. Lett.* **116** 054001
[24] Langford N K, Sagastizabal R, Kounalakis M, Dickel C, Bruno A, Luthi F, Thoen D J, Endo A and DiCarlo L 2017 *Nat. Commun.* **8** 1715
[25] Johnson B R 2011 *Controlling Photons in Superconducting Electrical Circuits*, Ph.D. Dissertation (New Haven: Yale University)
[26] Kelly J 2015 *Fault-tolerant superconducting qubits*, Ph.D. Dissertation (Santa Barbara: University of California, Santa Barbara)

[27] Cerfontaine P, Botzem T, DiVincenzo D P and Bluhm H 2014 *Phys. Rev. Lett.* **113** 150501
[28] Cerfontaine P, Botzem T, Ritzmann J, Humpohl S S, Ludwig A, Schuh D, Bougeard D and Wieck A D 2020 *Nat. Commun.* **11** 4144
[29] Cerfontaine P, Otten R and Bluhm H 2020 *Phys. Rev. Appl.* **13** 044071
[30] Andrews R W, Jones C, Reed M D, Jones A M, Ha S D, Jura M P, Kerckhoff J, Levendorf M, Meenehan S, Merkel S T, Smith A, Sun B, Weinstein A J, Rakher M T, Ladd T D and Borselli M G 2019 *Nat. Nanotechnol.* **14** 747
[31] Hu R Z, Ma R L, Ni M, Zhou Y, Chu N, Liao W Z, Kong Z Z, Cao G, Wang G L, Li H O and Guo G P 2023 *Appl. Phys. Lett.* **122** 134002
[32] Zhang X, Zhou Y, Hu R Z, Ma R L, Ni M, Wang K, Luo G, Cao G, Wang G L, Huang P, Hu X, Jiang H W, Li H O, Guo G C and Guo G P 2021 *Phys. Rev. Appl.* **15** 044042
[33] Zhang X, Hu R Z, Li H O, Jing F M, Zhou Y, Ma R L, Ni M, Luo G, Cao G, Wang G L, Hu X, Jiang H W, Guo G C and Guo G P 2020 *Phys. Rev. Lett.* **124** 257701
[34] Ni M, Ma R L, Kong Z Z, Xue X, Zhu S K, Wang C, Li A R, Chu N, Liao W Z, Cao G, Wang G L, Guo G C, Hu X, Jiang H W, Li H O and Guo G P 2023 arXiv: 2310.06700 [cond-mat]
[35] Yoneda J, Otsuka T, Takakura T, Pioro-Ladrière M, Brunner R, Lu H, Nakajima T, Obata T, Noiri A, Palmstrøm C J, Gossard A C and Tarucha S 2015 *Appl. Phys. Express* **8** 084401
[36] Russ M, Zajac D M, Sigillito A J, Borjans F, Taylor J M, Petta J R and Burkard G 2018 *Phys. Rev. B* **97** 085421
[37] Petta J R, Johnson A C, Taylor J M, Laird E A, Yacoby A, Lukin M D, Marcus C M, Hanson M P and Gossard A C 2005 *Science* **309** 2180